Power-flow-based Stabilization for Adaptive Feedforward Filters in Hybrid Testing

Andreas Bartl L.D. Hashan Peiris Jonathan L. du Bois Daniel J. Rixen
Andrew Plummer

June 10, 2020

Abstract

Real-time hybrid testing is a technology which allows the coupling of simulations and component tests in order to simulate complex system dynamics. Delays and time lags caused by actuator dynamics and signal processing deteriorate the stability of the tests in many cases. The application of adaptive feedforward filters to hybrid testing enables circumventing this problem. The stability of the filter itself, however, can be affected by the choice of the algorithm parameters or changes in dynamics of the system being tested. Test safety requirements and practical considerations require a failsafe implementation. In this paper, we propose a method for adjusting the parameters of the adaptive feedforward filter based on power-flows in the test setup. The objective is to maintain a passive behavior of the actuation and control system. The stabilization acts on the leakage factor and the adaptation gain of a least-mean-squares adaptation law. A simple numerical system is used to investigate the effect of the algorithm parameters on the stabilization. The method was applied to an experimental setup including a nonlinear stiffness. Several originally unstable configurations were stabilized, the adaptation process could be continued and interface synchronization was achieved in all test cases.

1 Introduction

Real-time hybrid testing—also referred to as real-time dynamic substructuring—is a method for implementing realistic dynamical tests of components of complex systems. The system is split into a virtual system—which is simulated in real time—and an experimental component which is physically present in the test. Applications of the method have been reported in various fields as in aerospace, automotive, civil and mechanical engineering. In literature, a large number of use cases have been described. To name only a few examples: Satellite tests using hybrid approaches are proposed in [5], [7] describes air-to-air refilling scenarios and [16] proposes the tests on chassis dynamics of cars in combination with aerodynamic simulations. The objective of any real-time hybrid testing technology is to test the experimental component under realistic boundary conditions. To do so, the dynamics of the virtual component are coupled to the test rig during the test, using an actuation system. Actuators apply forces to the interface of the experimental component, while sensors measure interface forces and interface displacements. Most test setups make time lags and delays inevitable. Frequency-dependent time lags are caused by the dynamics of the actuators. Delays are caused by the computational and communication processes as well as by signal-processing procedures. Time lags and delays can cause instability or inaccuracies if occurring in a test without a further compensation technique. To overcome these stability problems, a number of methods have been proposed in hybrid-testing literature. [10] suggests using a polynomial forward prediction scheme which compensates for delay and amplitude errors. Based on this work, [19] introduces an additional adaptation scheme which tunes phase shifts and amplitude corrections according to errors at the zero crossings. Other methods for delay compensation and interface synchronization include the application of model reference adaptive control by [18], inverted models of the actuation system by [6] and model predictive control by [17]. [14] applies a passivity based control method to real-time hybrid testing.

Fig. 1 gives an example of an application of hybrid tests to a structural dynamic system: The objective of the test is to analyze the influence of different designs of drive trains and transmission cross beams on

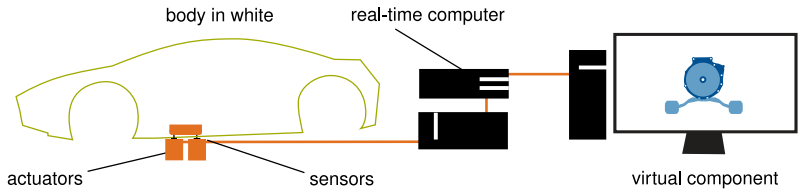

Figure 1: Application case: The virtual component can be optimized with respect to its effect on the body in white's vibrations.

the vibration behavior of a car. The body in white is a complex structure which is hard to model, while the transmission cross beam and the drive train are only available as models and their design frequently changes during the design process. A hybrid testing approach allows the coupling of the physical body in white to the model of the transmission system. Applications where structural systems are coupled often exhibit high modal density and low damping. This fact makes the application of feedback-based methodologies using low-order models challenging. Adaptive feedforward filters offer an alternative in this field. Instead of closing the control loop directly, feedforward filters generate the actuator input using the external excitation forces as an input signal. Since the structure of the filter is not known beforehand, information on the interface tracking error is used in an update law to adapt the filter coefficients such that virtual and experimental components are coupled. An approach based on feedforward filters has been applied to the testing of piezoelectric actuators in [8]. The application to problems with multiple degree-of-freedom interfaces has been addressed in [4].

The work in this paper is based on least-mean-square filters as it is described in [3]. Adaptation gains are parameters which define the aggressiveness of the adaptation of the filters. Despite the fact that adaptive feedforward-filter-based methods show more robust stability properties than their feedback counterparts, adaptation gains have to be selected with care. High adaptation gains, insufficient plant identification or changes in the system dynamics during the test can lead to unstable filter dynamics. We address the problem with an approach inspired by passivity-based techniques from the fields of teleoperation, force reflection, robotic impedance control, and haptic interfaces. These cases relate to hybrid testing, since in all problem settings physical systems are coupled via an actuation and sensing system, and delay and time lag frequently degenerate system performance. In teleoperation, the environment exhibits unknown dynamics and the communication link can show significant delays. Many works in this field employ passivity-based methods. The reason is that passivity is a sufficient condition for stability if all the other components in the system are also passive.

The stability of the system can be concluded from assessing the subsystems separately. Additionally, passivity theory is not limited to linear systems but applies to non-linear systems as well. A system is passive if the energy inflow is higher than the energy outflow for all the time. The work of [2] and [13] introduce passivity-based methods which utilize wave variables to make the communication line passive. Passivity-based methods have been applied to robotic impedance control such as e.g. in [1]. [9] proposes a control scheme for haptic interfaces which uses adaptive dissipative elements to ensure passivity. The technique presented in [14] is a passivity-based approach to hybrid testing. The method implements a variable rate virtual damping element to the numerical substructure to ensure the passivity of the transfer system. The damping-coefficient is controlled by the excess energy added to the hybrid system by the actuator.

In this paper, we propose a method which uses the power flow as a measure to update the adaptation parameters in the case of unstable behavior caused by a large adaptation gain set by the user. The technique restores filter stability and subsequently enables adaptation with accurate synchronization in all investigated test cases. The paper is organized as follows: Section II introduces a hybrid-testing method based on adaptive feedforward filters. The power flow supervision approach is presented in section III. Section IV gives an overview of the influence of the algorithm parameters using an exemplary numerical simulation. In section V, the experimental results of tests with a physical nonlinear spring arrangement are analyzed.

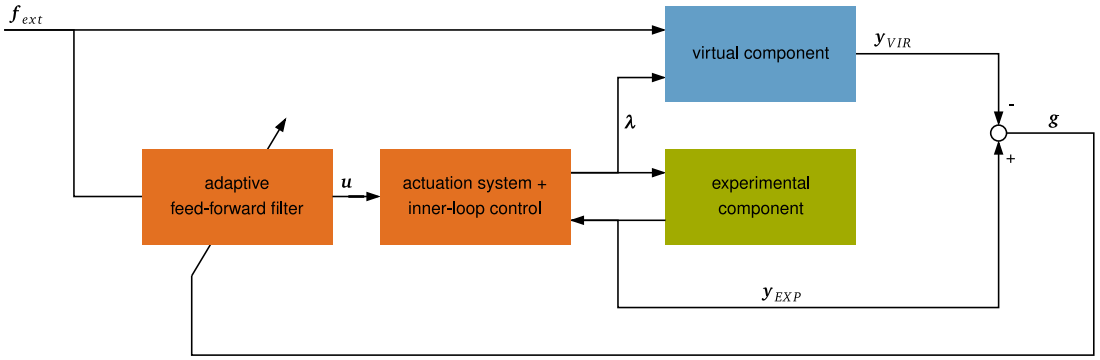

Figure 2: General control structure: Interface equilibrium is enforced by imposing the measured interface forces on the virtual component. A feedforward controller reduces the interface gap $\boldsymbol{g}$ such that the system meets the compatibility constraints. The arrow pointing back to the actuation system represents the mechanical interaction of the experimental component and the actuation system.

2 Coupling Problem and Adaptive Feedforward Filters

Coupling between virtual and experimental components is achieved if the interface displacements of the virtual and the experimental components match and if the interface forces are in equilibrium. In order to apply adaptive feedforward filters to the problem, we make use of the control structure depicted in Fig. 2. The equilibrium is imposed by applying the measured interface forces of the experimental component onto the virtual component. Using a controller, the interface compatibility constraint is then enforced by providing appropriate input to the actuation system to ensure the virtual and physical displacements match. Eqs. (1) describe the virtual component's dynamics with the symbols $\boldsymbol{M}^{VIR}$ $\boldsymbol{D}^{VIR}$ and $\boldsymbol{K}^{VIR}$ for mass, damping and stiffness matrices. The interface forces are denoted by $\boldsymbol{f}_b^{VIR}$. $\boldsymbol{G}^{VIR}$ is the matrix mapping the interface forces onto the system coordinates. The external excitation forces are denoted by $\boldsymbol{f}_{ext}^{VIR}$ and $\boldsymbol{f}_{ext}^{EXP}$. In the state-space form the dynamic equations are written using the system matrix $\boldsymbol{A}^{VIR}$, the input matrix for the interface forces $\boldsymbol{B}_{\lambda}^{VIR}$, the input matrix for the external forces $\boldsymbol{B}_{ext}^{VIR}$ and the state vector $\boldsymbol{x}^{VIR}$. The interface displacement is $\boldsymbol{y}^{VIR}$ and the output matrix is denoted by $\boldsymbol{C}_y^{VIR}$.

$$\begin{aligned}\dot{\boldsymbol{x}}^{VIR} &= \underbrace{\begin{bmatrix}\boldsymbol{0} & \boldsymbol{I}\\ -\boldsymbol{M}^{VIR-1}\boldsymbol{K}^{VIR} & -\boldsymbol{M}^{VIR-1}\boldsymbol{D}^{VIR}\end{bmatrix}}_{\boldsymbol{A}^{VIR}}\boldsymbol{x}^{VIR} + \underbrace{\begin{bmatrix}\boldsymbol{0}\\ \boldsymbol{M}^{VIR-1}\boldsymbol{G}^{VIRT}\end{bmatrix}}_{\boldsymbol{B}_{\lambda}^{VIR}}\boldsymbol{f}_b^{VIR} + \underbrace{\begin{bmatrix}\boldsymbol{0}\\ \boldsymbol{M}^{VIR-1}\end{bmatrix}}_{\boldsymbol{B}_{ext}^{VIR}}\boldsymbol{f}_{ext}^{VIR}\\ \boldsymbol{y}^{VIR} &= \boldsymbol{C}_y^{VIR}\boldsymbol{x}^{VIR}\end{aligned} \tag{1}$$

Being assembled in the test rig, the experimental component may influence the dynamics of the actuation system. Using the coupled dynamics of the actuation system and the experimental component in the following accounts for this feedback. Note that the actuation system may contain an inner-loop control with actuator-specific features such as friction compensation. Eqs. (2) describe the dynamics of the actuation system and the experimental component in state-space form:

$$\begin{aligned}\dot{\boldsymbol{x}}^{EXP} &= \boldsymbol{A}^{EXP}\boldsymbol{x}^{EXP} + \boldsymbol{B}_u^{EXP}\boldsymbol{u} + \boldsymbol{B}_{ext}^{EXP}\boldsymbol{f}_{ext}^{EXP}\\ \boldsymbol{y}^{EXP} &= \boldsymbol{C}_y^{EXP}\boldsymbol{x}^{EXP}\\ \boldsymbol{\lambda} = \boldsymbol{f}_b^{EXP} &= \boldsymbol{C}_{\lambda}^{EXP}\boldsymbol{x}^{EXP} + \boldsymbol{D}_u^{EXP}\boldsymbol{u} + \boldsymbol{D}_{ext}^{EXP}\boldsymbol{f}_{ext}^{EXP}\end{aligned} \tag{2}$$

Here $\boldsymbol{A}^{EXP}$, $\boldsymbol{B}_u^{EXP}$, $\boldsymbol{B}_{ext}^{EXP}$, $\boldsymbol{C}_y^{EXP}$, $\boldsymbol{C}_{\lambda}^{EXP}$, $\boldsymbol{D}_u^{EXP}$ and $\boldsymbol{D}_{ext}^{EXP}$ are the the state-space matrices, and $\boldsymbol{x}^{EXP}$ is the state vector. The inputs to the system are the actuator demand signal $\boldsymbol{u}$ and the external forces acting on the experimental component. The interface displacement of the experimental component $\boldsymbol{y}^{EXP}$ and the interface forces $\lambda = \boldsymbol{f}_b^{EXP}$, namely the inner forces between the virtual and experimental substructures, are defined as the outputs of the system.
This state-space equations represent the general form of the experimental component. In order to make the derivation of the adaptive filter clearer a linear dynamical system is assumed at this point.

The open-loop dynamics—which are later controlled such that the compatibility constraint is met—are given by Eq. (3). The interface force vector $\boldsymbol{f}_b^{VIR}$ is eliminated by applying the output of the actuation system to the virtual component. In practice, this involves measuring the interface forces between the actuator system and the experimental component. We refer to the equilibrium interface forces as $\boldsymbol{\lambda}$.

$$\boldsymbol{\lambda} = \boldsymbol{f}_b^{EXP} = -\boldsymbol{f}_b^{VIR} \tag{3}$$

Actuator demand and external forces on both subcomponents are defined as system inputs, and the interface gap $\boldsymbol{g}$ is defined as system output. The interface gap $\boldsymbol{g}$ is the difference between the virtual component's and the experimental component's interface displacements.

$$\begin{aligned} \dot{\boldsymbol{x}} &= \underbrace{\begin{bmatrix} \boldsymbol{A}^{VIR} & \boldsymbol{B}_\lambda^{VIR}\boldsymbol{C}_\lambda^{EXP} \\ \boldsymbol{0} & \boldsymbol{A}^{EXP} \end{bmatrix}}_{\boldsymbol{A}} \boldsymbol{x} + \underbrace{\begin{bmatrix} \boldsymbol{B}_\lambda^{VIR}\boldsymbol{D}_u^{EXP} \\ \boldsymbol{B}_u^{EXP} \end{bmatrix}}_{\boldsymbol{B}_u} \boldsymbol{u} + \underbrace{\begin{bmatrix} \boldsymbol{B}_{ext}^{VIR} & \boldsymbol{B}_\lambda^{VIR}\boldsymbol{D}_{ext}^{EXP} \\ \boldsymbol{0} & \boldsymbol{B}_{ext}^{EXP} \end{bmatrix}}_{\boldsymbol{B}_{ext}} \boldsymbol{f}_{ext} \\ \boldsymbol{g} &= \underbrace{\begin{bmatrix} \boldsymbol{C}_y^{VIR} & -\boldsymbol{C}_y^{EXP} \end{bmatrix}}_{\boldsymbol{C}} \boldsymbol{x} \quad with \quad \boldsymbol{x} = \begin{bmatrix} \boldsymbol{x}^{VIR^T} & \boldsymbol{x}^{EXP^T} \end{bmatrix}^T \quad and \quad \boldsymbol{f}_{ext} = \begin{bmatrix} \boldsymbol{f}_{ext}^{VIR^T} \boldsymbol{f}_{ext}^{EXP^T} \end{bmatrix}^T \end{aligned} \tag{4}$$

Eqs. (5) shows the time-domain solution of interface gap $\boldsymbol{g}$. The solution is a combination of contributions from actuator input, external forces and initial conditions. The contributions from the actuator input and the external forces can be expressed as convolutions between the impulse responses $\boldsymbol{h}_u$ and $\boldsymbol{h}_{exp}$ and the inputs.

$$\boldsymbol{g}(t) = \int_{t_0}^{t} \underbrace{\boldsymbol{C}e^{\boldsymbol{A}(t-\tau)}\boldsymbol{B}_u}_{\boldsymbol{h}_u(t-\tau)} \boldsymbol{u}(\tau)d\tau + \int_{t_0}^{t} \underbrace{\boldsymbol{C}e^{\boldsymbol{A}(t-\tau)}\boldsymbol{B}_{ext}}_{\boldsymbol{h}_{ext}(t-\tau)} \boldsymbol{f}_{ext}(\tau)d\tau + \boldsymbol{C}e^{\boldsymbol{A}t}\boldsymbol{x}(t_0) \tag{5}$$

The objective of any controller is to close the interface gap. In many applications, as rotation machinery or drive trains, harmonic excitation occurs. The harmonic excitation force $\boldsymbol{f}_{ext}(t)$ with the excitation frequencies Ω_i and $i \in [1 \dots n_{ext}]$ is given in Eq. (6).

$$\boldsymbol{f}_{ext}(t) = \sum_{i=1}^{n_{ext}} \boldsymbol{a}_i \cos(\Omega_i t) + \boldsymbol{b}_i \cos(\Omega_i t) \tag{6}$$

Assuming steady-state and harmonic excitation, the interface gap can be closed by applying a harmonic signal as the actuator input. The actuator input in Eq. (7) is constructed by the multiplication of a harmonic basis function matrix $\boldsymbol{W}(t)$ and the parameter vector $\boldsymbol{\theta}$. The matrix $\boldsymbol{W}(t)$ contains sinusoidal functions using the excitation frequencies and their multiples. The total number of frequencies contained in the basis function matrix $\boldsymbol{W}(t)$ is n_Ω. Using multiples of the excitation frequencies in the basis functions higher harmonics in weakly nonlinear systems can be compensated for. The parameter vector controls amplitude and phase of the actuator input signal $\boldsymbol{u}$. Note that we use the time-discrete form of the signals which can be retrieved by setting in $t = k\Delta t$ with time instance k and time-step width Δt. The number of the time instance is indicated with square brackets.

$$\boldsymbol{u}[k] = \underbrace{\begin{bmatrix} \boldsymbol{I}\cos\Omega_1 k\Delta t \\ -\boldsymbol{I}\sin\Omega_1 k\Delta t \\ \vdots \\ \boldsymbol{I}\cos\Omega_{n_\Omega} k\Delta t \\ -\boldsymbol{I}\sin\Omega_{n_\Omega} k\Delta t \end{bmatrix}^T}_{\boldsymbol{W}[k]} \boldsymbol{\theta}[k] \tag{7}$$

Using the Fourier transform $\mathcal{F}(\boldsymbol{h}_u(t)) = \boldsymbol{H}_u(\omega)$ of the impulse response $\boldsymbol{h}_u(t)$ and neglecting the transient terms, the interface gap $\boldsymbol{g}(t)$ can be written in the matrix-vector form of Eq. (8). A proof is shown in [4]. The expression contains the basis function matrix $\boldsymbol{W}(t)$, the transfer function matrix $\boldsymbol{P}_{gu}$ and the parameter vector $\boldsymbol{\theta}$ as well as the contribution of the external excitations $\boldsymbol{g}_{ext}$ to the interface gap. The objective of the adaptation law is now to find a parameter vector $\boldsymbol{\theta}$ such that the interface gap $\boldsymbol{g}(t)$ is

minimized.

$$\boldsymbol{g}[k] = \boldsymbol{W}[k] \underbrace{\begin{bmatrix} Re(\boldsymbol{H}_u(\Omega_1)) & -Im(\boldsymbol{H}_u(\Omega_1)) & & & \\ Im(\boldsymbol{H}_u(\Omega_1)) & Re(\boldsymbol{H}_u(\Omega_1)) & & & \\ & & \ddots & & \\ & & & Re(\boldsymbol{H}_u(\Omega_{n_\Omega})) & -Im(\boldsymbol{H}_u(\Omega_{n_\Omega})) \\ & & & Im(\boldsymbol{H}_u(\Omega_{n_\Omega})) & Re(\boldsymbol{H}_u(\Omega_{n_\Omega})) \end{bmatrix}}_{\boldsymbol{P}_{g,u}} \boldsymbol{\theta}[k] + \boldsymbol{g}_{ext}[k], \tag{8}$$

where $\boldsymbol{g}_{ext}[k]$ is the contribution of the external excitations. Eq. (9) gives the objective function for the adaptation law which is the sum of the squared interface gap and a regularization term. The regularization term contains the squared parameter vector $\boldsymbol{\theta}$ and the regularization parameter γ.

$$J[k] = \boldsymbol{g}^T[k]\boldsymbol{g}[k] + \gamma\boldsymbol{\theta}^T\boldsymbol{\theta} \tag{9}$$

The least-mean-squares (LMS) update law for the parameter vector $\boldsymbol{\theta}$ given in Eq. (10) is basically a gradient descent algorithm. In contrast to feedback controllers as e.g. classical LQR control, the actuator input is generated using a sinusoidal basis function with defined frequencies and the parameter vector. The gradient of the objective function can be calculated using the transfer matrix $\boldsymbol{P}_{gu}$, the basis function matrix $\boldsymbol{W}(t)$ and the interface gap $\boldsymbol{g}$. The adaptation gain $\bar{\mu}$ controls the convergence speed of the adaptation process. High values of $\bar{\mu}$ may result in an unstable adaptation process. The leakage factor ν stems from the regularization term in the objective function. In this paper, the leakage factor is used to reduce the filter coefficient in the case of an unstable behavior. Besides a choice of $\bar{\mu}$ the matrix $\boldsymbol{P}_{gu}$ is critical to the stability and the quality of the adaptation process. Since the actual values of matrix $\boldsymbol{P}_{gu}$ are not known beforehand, the matrix has to be estimated. Usually $\boldsymbol{P}_{gu}$ is identified in an identification phase which precedes the adaptation phase. Errors in the identification or changes in the system dynamics can lead to the instability of the adaptation process.

$$\boldsymbol{\theta}[k+1] := \nu\boldsymbol{\theta}[k] - \bar{\mu}\boldsymbol{P}_{g,u}^T\boldsymbol{W}[k]^T\boldsymbol{g}[k] \qquad with \qquad \nu = 1 - \bar{\mu}\gamma \tag{10}$$

In order to make the choice of the adaptation gain more practicable, we use a normalized adaptation gain μ according to Eq. (11). The normalization makes use of the maximum eigenvalue λ_{max} of the matrix $\boldsymbol{P}_{g,u}^T\boldsymbol{P}_{g,u}$. See e.g. [12] for a derivation of the expressions. In theory, a normalized adaptation gain of $\mu = 1$ results in the fastest possible convergence. Changes in the system dynamics and inaccuracy in the identification process may bring the maximum adaptation gain down to a lower value.

$$\bar{\mu} = \mu\frac{1}{\lambda_{max} + \gamma} \tag{11}$$

3 Power-flow Supervision

In order to overcome the aforementioned stability issues, we propose the use of a supervisor which reduces the adaptation gain μ whenever necessary. To do so, we analyze the power-flows between the subcomponents. Those power-flows are closely linked to passivity properties of the hybrid test. Passive systems are defined as systems which consume energy but do not produce energy. Coupling two arbitrary passive systems results in a passive overall system.

One can think of the control system and actuation system of a hybrid test as an interconnection device between the virtual and the experimental component. We refer to this combination of the control system and the actuation system as the "transfer system" in this section. In the case that the transfer system is passive , energy is only injected into the test setup through external forcing on the virtual or the experimental component but not through the transfer system. The transfer system is referred to as "passive" if the power-inflow into the system is always larger than the power-outflow. The power-inflow P_{in}^{ACT} to the transfer system is the sum of the power-inflow from the experimental component and the power-inflow from the virtual component. Both are the product of collocated interface forces and interface velocities. As a result, the power-inflow to the transfer system in Eq. (12) is the product of interface forces and the time derivative of the interface gap.

$$P_{in}^{ACT} = \boldsymbol{f}_b^{VIR}\dot{\boldsymbol{y}}^{VIR} + \boldsymbol{f}_b^{EXP}\dot{\boldsymbol{y}}^{EXP} = -\boldsymbol{\lambda}\dot{\boldsymbol{y}}^{VIR} + \boldsymbol{\lambda}\dot{\boldsymbol{y}}^{EXP} = \boldsymbol{\lambda}\dot{\boldsymbol{g}} \tag{12}$$

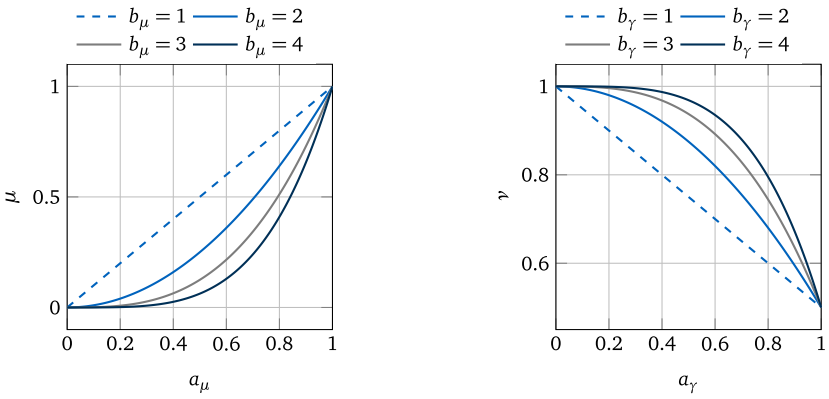

Figure 3: Parameter adjustment functions

A negative power-inflow into the transfer system—or in other words a power-outflow from the transfer system—implies undesirable energy injection into the hybrid test. In order constrain the power-outflow of the transfer system which deteriorates its passive nature, we introduce a limit to the power-outflow P_{lim}. The limit $P_{lim} < 0$ is a negative value specific to the required power-outflow limit of the test. The objective of the power-flow supervision is to constrain the power-flow according to Eq. (13).

$$\lim_{t\to\infty} P_{in}^{ACT} \geq P_{lim} \tag{13}$$

Note that the energy inflow is defined as the time integral of the power-inflow:

$$E_{in}^{ACT} = \int_0^t P_{in}^{ACT}(\tau) d\tau$$

Following a simple heuristic approach, as a result of the violation of the passivity constraint, the two parameters μ and γ of the adaptation algorithm are adjusted. The objective is to reduce the actuator amplitudes, to restore passivity and to enable fast adaptation. Approaches such as [11] where the leakage factor is adjusted according to the algorithm's performance have been proposed in literature. The stability and the convergence of the least-mean-squares algorithm is controlled by the adaptation gain μ: A high adaptation gain μ leads to a fast convergence of the filter coefficients, but high values can lead to the unstable behavior of the algorithm. In contrast, lower values of μ cause a slower convergence but stability is ensured if the value falls below the stability threshold. As a consequence, the adaptation gain μ is reduced using the exponential function in Eq. (14) with the initial adaptation gain μ_{init}, the variable a_μ and the user-defined exponent $b_\mu \geq 1$. The reasons for using an exponential function are to enable a faster drop of the adaptation gain μ in the initial phase, to ensure a fast restoration of passivity and a slower change in μ if it is closer to its optimal value. Fig. 3 shows the functions for some exemplary values b_μ.

$$\mu = \mu_{init} \cdot a_\mu^{b_\mu} \qquad \Rightarrow \qquad \mu \in [0,\ \mu_{init}] \quad \forall \quad a_\mu \in [0,\ 1] \tag{14}$$

The initial value is $a_\mu = 1$. If the power-inflow to the actuation system falls below the threshold P_{lim}—meaning that the system is not passive—the variable a_μ is reduced by the user-defined step-size parameter $\Delta_\downarrow a_\mu$. The lower bound for the variable a_μ is zero. As a result, the adaptation gain is bound by zero and the initial adaptation gain μ_{init}. The leakage factor ν results from the regularization factor γ according to Eq. (10). A low leakage factor—or equivalently, a high regularization factor—enforces lower filter coefficients. It is desirable to reduce the filter coefficients after a violation of the passivity constraint is detected. After the passive state is restored by the drop in the adaptation gain μ, the regularization should be reduced to ensure that the filter coefficients are adapted accurately to their optimal values. The regularization parameter γ is calculated using the exponential function in Eq. (15) with the user-defined maximum regularization factor γ_{max}, the variable a_γ and the user-defined exponent $b_\gamma \geq 1$. Fig. 3 shows the functions for some exemplary values b_γ. The nature of the exponential function leads to a progressive behavior of the leakage: In cases of severe power-outflow,

Table 1: System parameters used in the numerical case study

Virtual Component (VIR)		Experimental Component (EXP)		Actuator (ACT)	
m^{VIR}	$0.1\,kg$	m^{EXP}	$0.02\,kg$	m^{ACT}	$0.1\,kg$
d^{VIR}	$0.05\,\frac{N\cdot s}{m}$	d^{EXP}	$0.05\,\frac{N\cdot s}{m}$	d^{ACT}	$1\,\frac{N\cdot s}{m}$
k^{VIR}	$1000\,\frac{N}{m}$	k^{EXP}	$1000\,\frac{N}{m}$	k^{ACT}	$100\,\frac{N}{m}$

the filter coefficients fall faster.

$$\gamma = \gamma_{max} \cdot a_\gamma^{b_\gamma} \qquad \Rightarrow \qquad \nu \in [1 - \bar{\mu}\,\gamma_{max},\ 1] \quad \forall \quad a_\gamma \in [0,\ 1] \tag{15}$$

The initial value is $a_\gamma = 0$. If the power-inflow to the actuation system P_{in}^{ACT} falls below the threshold P_{lim}—meaning that the system is not passive—the variable a_γ is increased by the user-defined step-size parameter $\Delta_\uparrow a_\gamma$. If the power-inflow to the actuation system P_{in}^{ACT} rises above the threshold P_{lim}—meaning that the system is assumed to be passive—the variable a_γ is reduced by the user-defined step-size parameter $\Delta_\downarrow a_\gamma$. The lower bound for the variable a_γ is zero and the upper bound is 1. As a result, the adaptation gain is bound by one and $1 - \bar{\mu}\,\gamma_{max}$. The complete procedure including the adaptation of μ and ν is summarized in the pseudo-code of Alg. 1.

Algorithm 1 Power supervision for adaptive feedforward filters in hybrid testing

```
Initialize a_γ := 0 and a_μ := 1
while adaptation is running do
    if P_in^ACT < P_lim then
        Set a_γ := min(a_γ + Δ_↑ a_γ, 1)
        Set a_μ := max(a_μ − Δ_↓ a_μ, 0)
    end if
    if P_in^ACT > P_lim then
        a_γ := max(a_γ − Δ_↓ a_γ, 0)
    end if
    Set γ := γ_max · a_γ^{b_γ}
    Set μ := μ_init · a_μ^{b_μ}
end while
```

4 Numerical Example of Choice of the Algorithm's Parameters

In order to demonstrate the effects of changes in the adaptation parameters a_μ and b_μ as well as the power-inflow limit P_{lim}, we make use of a simple numerical test case. The overall system emulated in the test is a lumped mass-spring-damper system as shown in Fig. 4. The system is split into a virtual component and an experimental component. In Fig. 4 the virtual component is depicted in blue and the experimental component is depicted in green. The experimental component is controlled via an actuation system, which is depicted in orange in Fig. 4. The actuator and its controller are modeled as a second order response with equivalent mechanical properties. The properties of the subsystems are listed in Tab. 1. Since the adaptive feedforward filter acts exactly at the excitation frequencies measurement noise can cause a drift of the interface gap. A peak filter using the excitation frequency was applied at the actuator input in order to prevent those drift effects. The objective of the first numerical experiment is to investigate the influence of the changes in $\Delta_\downarrow a_\mu$. To do so, we varied the parameter $\Delta_\downarrow a_\mu$ while keeping all other parameters constant. Tab. 2 gives an overview of the parameters. Note that the initial adaptation-gain $\mu_{init} = 10$ is a high value, which causes an unstable system behavior without the passivity-preserving mechanism. As mentioned earlier, such instabilities can be caused in exactly the same way by an insufficient system identification process as well as by changes in the system parameters. The simulation includes a 50 s identification phase. The identification was performed

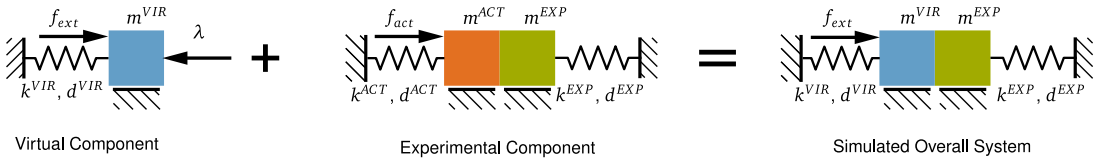

Figure 4: Lumped mass system used for the numerical experiment

Table 2: Parameters for the numerical experiment different adaptation-gain step-sizes $\Delta_{\downarrow} a_{\mu}$

Variable		Values
step-size	$\Delta_{\downarrow} a_{\mu}$	0.001
initial adaptation-gain	μ_{init}	10
exponent	b_{μ}	10
step-size	$\Delta_{\downarrow} a_{\gamma}$	0.001
step-size	$\Delta_{\uparrow} a_{\gamma}$	0.01
initial regularization factor	γ_{max}	1
exponent	b_{γ}	2
power-generation limit	P_{lim}	$-1\,W$
excitation amplitude	A_{ext}	$10\,N$
excitation frequency	f_{ext}	$50\,Hz$

according to the procedure which is described in [4], where the adaption algorithm was used to find the transfer function of the system. The long duration of the identification phase is chosen to rule out as much as possible the influences of identification errors on the simulation.
Fig. 6 shows the leakage factor ν, the power-inflow P_{in}^{ACT} to the actuator system, and the envelope of the interface gap $\boldsymbol{g}$. Note that the power-inflow is normalized with the peak values of the power-inflow into the reference system $P_{in,max}^{REF}$, the energy-inflow is normalized with the peak values of the energy in the reference system E_{max}^{REF} and the interface gap is normalized with the amplitude of displacement of the reference system y_{amp}^{REF}. It is noteworthy that the total energy outflow is highest for the lowest step-size values $\Delta_{\downarrow} a_{\mu}$. The interface gap is a measure for the synchronization of the interface between the virtual component and the experimental component. With increasing values of the step-size $\Delta_{\downarrow} a_{\mu}$, the interface gap gradually decreases. The reason is that lower choices for the step-size $\Delta_{\downarrow} a_{\mu}$ result in higher amplitudes at the start of the adaptation phase. The higher resulting adaptation-gain μ, however, may result in a faster convergence later in the test.

Fig. 5 shows the development of the adaptation-gain μ for variations of $\Delta_{\downarrow} a_{\mu}$, $\Delta_{\downarrow} a_{\gamma}$ and P_{lim}. As expected, the decay rate of the adaptation-gain is higher for higher step-sizes $\Delta_{\downarrow} a_{\mu}$. The adaptation-gain reduction is activated when the passivity constraint is violated. Depending on the reduction step-size $\Delta_{\downarrow} a_{\mu}$, the adaptation-gain may overstep the optimal adaptation-gain or reach it gradually. The resulting adaptation-gains for the passive state vary: Higher step-sizes $\Delta_{\downarrow} a_{\mu}$ result in a lower end value. Lower step-sizes $\Delta_{\downarrow} a_{\mu}$ exhibit a slower decay of the adaptation-gain but result in μ being closer to the optimal value.
The third graph Fig. 5 shows a variation of leakage factor step size. Higher step-sizes result in a larger drop in the leakage-factor. Since the lower leakage-factors reduce further power-outflow, the drop in the adaptation-gain μ is steeper and it settles faster for lower step-sizes $\Delta_{\uparrow} a_{\gamma}$.
The third graph Fig. 5 shows a variation of the power limit P_{lim}. The curves for μ are shifted in time since the different values of P_{lim} trigger the reduction of the adaptation-gain at different points in time. Slopes and final values of μ are not affected significantly by the choice of P_{lim}.

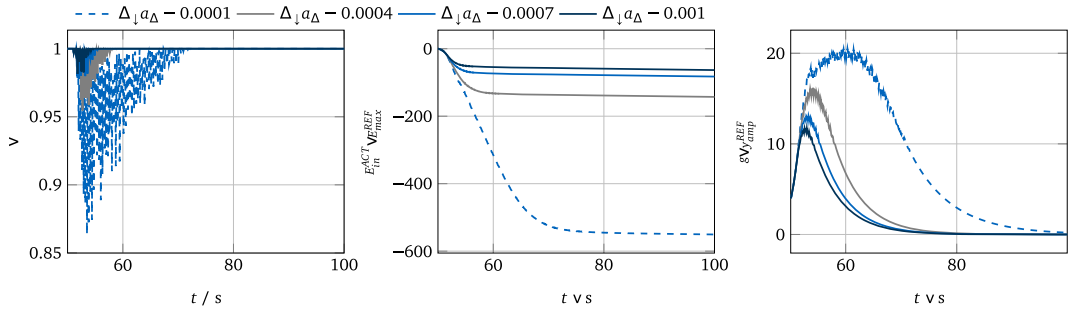

Figure 5: Leakage factor, power inflow to actuator system and learning curve for varying adaptation-gain step-sizes $\Delta_{\downarrow} a_{\mu}$

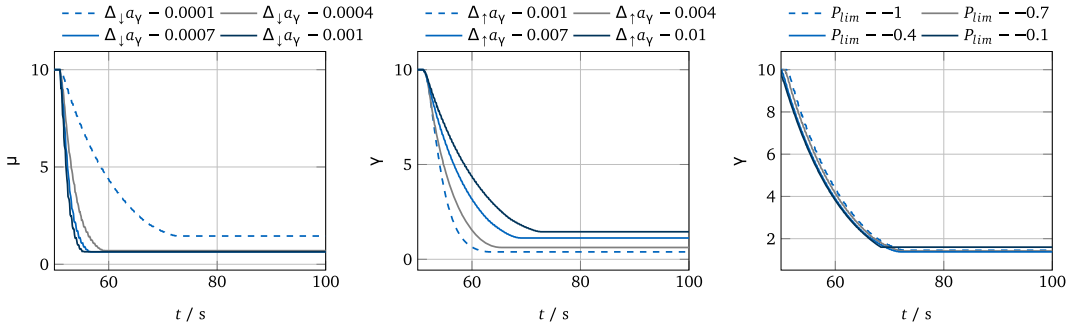

Figure 6: Development of the adaption gain for different parameters.

5 Experimental Validation

For the experimental validation of the approach, we use an approximation to a cubic spring as a physical subcomponent and a linear lumped-mass system as a virtual subcomponent. The test setup is depicted in Fig. 7. The cubic spring, which performs as the experimental component, is achieved using two linear springs with all forces acting perpendicular to the initial spring axis. The expression for the spring force is given by Eq. (16). The spring constants k_3^{EXP} and k^{EXP} were identified using a least-mean-squares fit. They are given in Tab. 3.

$$f^{EXP} = k_3^{EXP} x^3 + k^{EXP} x \tag{16}$$

The virtual component is a mass-spring-damper system and receives the external forces. A linear actuator—a Copley ST2508S electromagnetic linear actuator—applies the coupling forces to the experimental component. The actuator is controlled using a cascaded control scheme acting with a

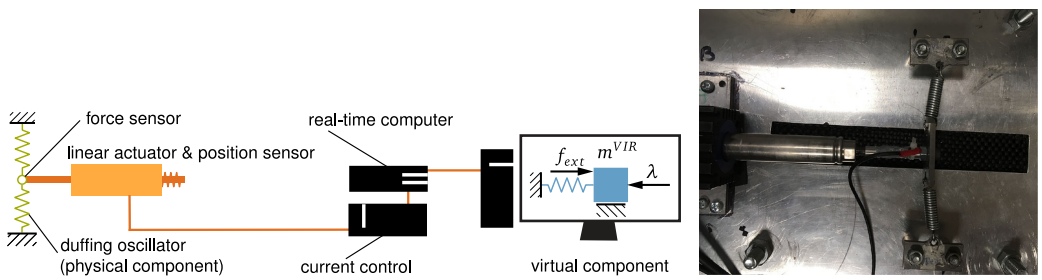

Figure 7: Test setup for the experimental validation of the approach

Table 3: System parameters of the experimental setup

Virtual Component (VIR)	
m^{VIR}	$1\,kg$
d^{VIR}	$10\,\frac{N\cdot s}{m}$
k^{VIR}	$1000\,\frac{N}{m}$

Experimental Component (EXP)	
k^{EXP}	$1.95\,\frac{N}{m}$
k_3^{EXP}	$0.0014\,\frac{N}{m^3}$

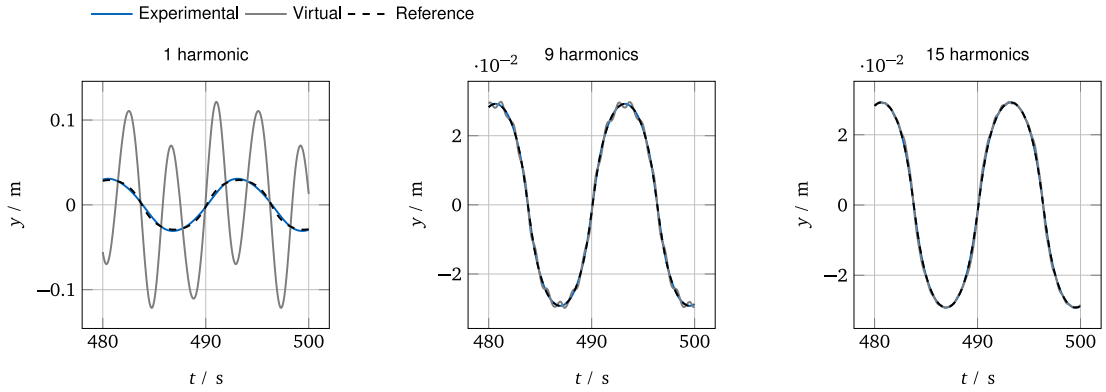

Figure 8: Exemplary interface displacements for excitation frequency 0.5 Hz and varying number of harmonics in basis function space. The excitation frequency was chosen such that the nonlinear behavior can be observed. In the first plot with one harmonic, the higher harmonic in the virtual component are excited through the interface forces but the higher harmonic interface displacement are not synchronized.

proportional term on the position demand, and with a proportional and integral term on the velocity demand. Friction has a significant effect on the actuator dynamics and, due to its non-linear nature the performance of hybrid-testing control schemes deteriorates. For that reason, a friction compensation scheme (as described in [15]) is implemented which acts on the input to the current control loop.
The actuator operates with a position saturation at $2.5 \cdot 10^{-2}\ m$ around the initial position for safety reasons. The interface forces are measured using a custom-made force sensor. Since the adaptive feedforward filter exactly at the excitation frequencies measurement noise can cause a drift of the interface gap. A peak filter using the excitation frequency was applied at the actuator input in order to prevent those drift effects. The position is measured using the internal sensor of the linear actuator. The coupled system exhibits nonlinear dynamics due to the nature of the spring assembly and uncompensated nonlinear friction in the actuator. If this setup is excited with one harmonic component, the response will contain higher harmonics. The presence of these higher harmonics, in general, requires the enrichment of the basis function space with higher harmonics. This means that the frequencies Ω_k of the harmonics in the basis function matrix $\boldsymbol{W}[k]$ are defined as multiples of the periodic excitation basis frequency Ω_0:

$$\Omega_k = k\Omega_0 \qquad with \qquad k \in [1,2,...,n_\Omega]$$

Fig. 8 shows the effect of the additional harmonics in the basis function matrix of the simulated system. However, for the excitation frequencies and amplitudes described in this section, one harmonic basis function is sufficient to couple the virtual and the experimental component satisfactorily. Note that the proposed approach is applicable to any number of harmonics in the basis function matrix. The test is performed keeping the parameters $\Delta_\downarrow a_\mu$, $\Delta_\downarrow a_\gamma$, $\Delta_\uparrow a_\gamma$, b_μ, b_γ, γ_{max} and P_{lim} constant. As mentioned above, one harmonic was used in the basis function matrix $\boldsymbol{W}[K]$. The excitation frequencies Ω_0 are varied. The excitation amplitudes were adjusted to the excitation frequencies because the resulting response amplitudes had to remain within the actuator workspace. The initial adaptation-gain μ_{init} was selected such that the resulting adaptation process is unstable without the proposed algorithm. Since we want to validate the performance of the power-flow supervision, the test for each frequency was performed in two modes: one using power-flow supervision and one using the pure adaptive feedforward

Table 4: Parameters used in the experiment

Variable			Values	
step size	$\Delta_{\downarrow} a_{\mu}$		0.001	
initial adaptation-gain	μ_{init}		0.1	
exponent	b_{μ}		2	
step size	$\Delta_{\downarrow} a_{\gamma}$		0.001	
step size	$\Delta_{\uparrow} a_{\gamma}$		0.01	
initial regularization factor	γ_{max}		1	
exponent	b_{γ}		2	
power-generation limit	P_{lim}		$-0.3\,W$	
excitation amplitude	A_{ext}	$10N$	$40N$	$40N$
excitation frequency	f_{ext}	$10Hz$	$20Hz$	$30Hz$

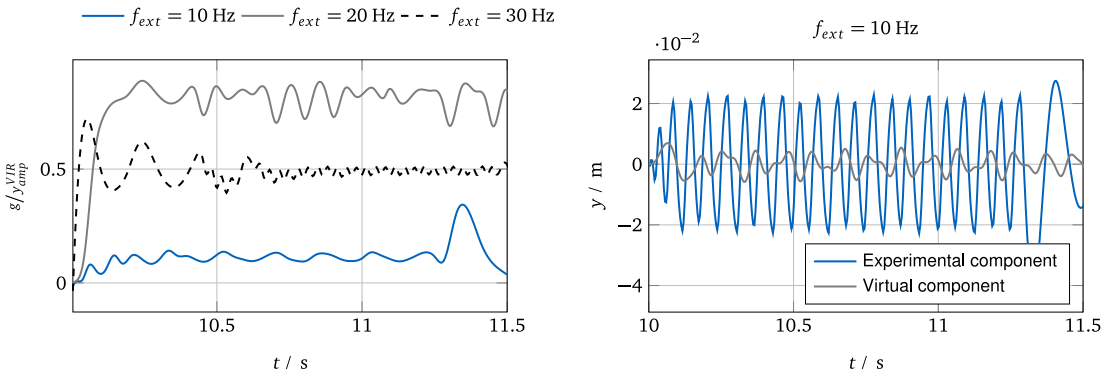

Figure 9: Unstable learning curve (left) and interface synchronization (right) without power-flow supervision.

control law without power-flow supervision. In the first experiment the adaptive feedforward filter approach is applied without power-flow-based stabilization. As a result, the adaptation-gain μ and the leakage factor ν stay constant throughout the test. Due to the selection of the adaptation-gain μ, the dynamics of the filter are expected to be unstable. Fig. 9 shows the interface gap as well as the time-domain synchronization plots for all excitation frequencies. In all cases, unstable filter dynamics can be observed. The actuator operates in a state of saturation and the responses show distorted peaks. Fig. 10 exhibits the high power- and energy-outflow from the actuator system caused by the instability.

The power-flow-based stabilization algorithm is activated in the second experiment. The adaptation-gains μ in Fig. 11 correspondingly drops to a value which allows the stable operation of the filter. The leakage factor ν also drops to values of 0 in the phases where the power-flow constraint is violated. Fig. 12 shows the power and energy outflow due to the initially unstable behavior. The maximum power-outflow is constrained to approximately $3\,W$. In the energy-outflow plot, a slight energy outflow can be observed after the stabilization of the test. The reason for this effect is stick-slip friction effects which are not compensated for by the actuator control. The remaining interface gap may cause the energy outflow which does not result in a unstable behavior. Finally, learning curve and time-domain synchronization plots in Fig. 13 show the stabilization effect of the proposed algorithm: Despite the fact that displacement peaks initially occur, the system is stabilized after a timespan of less than $0.5\,s$. After the stabilization, the adaptation continues and results in a synchronization between the virtual and the experimental component. Note that the displacement peaks can be prevented in a practical application by the application of a peak or comb filter to the actuator input. To summarize, the proposed approach enables the stabilization of an initially unstable test with a nonlinear spring. After stabilization, the

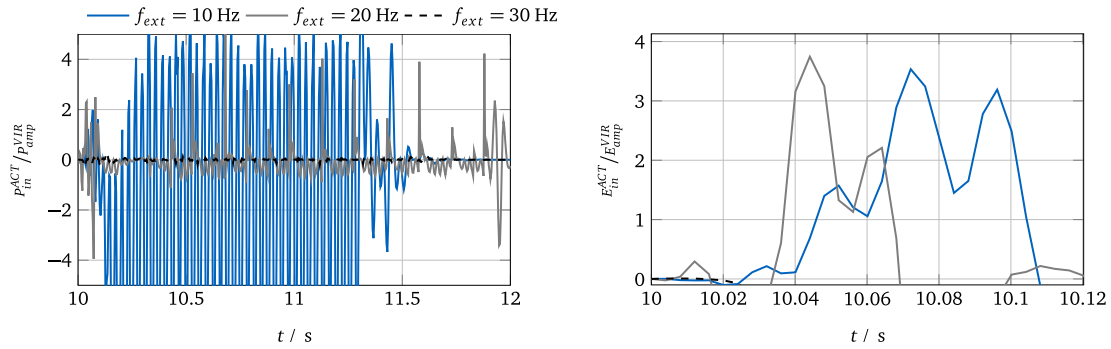

Figure 10: Unstable power (left) and energy inflow (right) to actuator system without power-flow supervision. The interface gap is normalized with the amplitude of the uncoupled interface displacement y_{amp}^{VIR}.

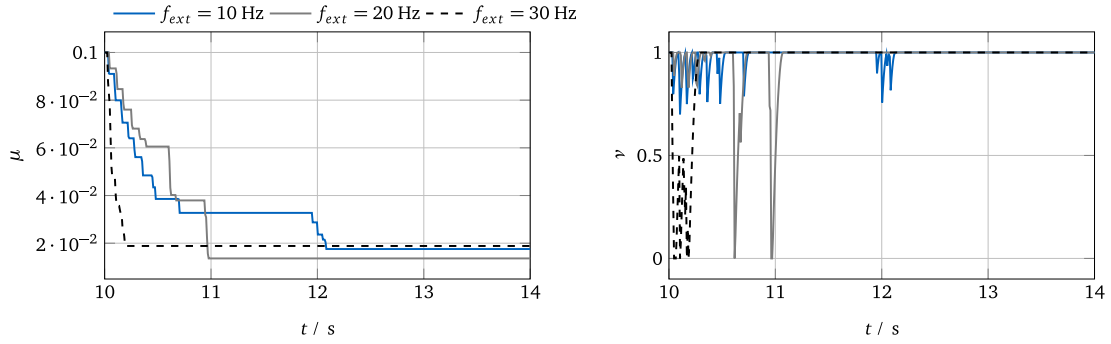

Figure 11: Adaptation gain (left) and leakage factor (right) with activated power-flow supervision

adaptation-gain settles and the system finally reaches interface synchronization.

6 Conclusion

In this paper, we propose a method to update the parameters of an adaptive feedforward filter in a hybrid test based on the power-outflow from the actuator and control system. In order to investigate the influence of the algorithm's parameters, we make use of a simple purely numerical case. The study leads to the following conclusions:

- Step size $\Delta_{\downarrow} a_{\mu} \in [0,\ 1]$ defines the convergence speed of the adaptation gain μ. High values can lead to lower values of μ.
- Step size $\Delta_{\uparrow} a_{\gamma} \in [0,\ 1]$ defines the convergence speed of the leakage factor ν. Higher values can reduce the peak values of power-outflow but increase the settling time.
- The power-outflow limit P_{lim} has only a slight influence on the final value of the adaptation gain but higher values reduce the peak interface gap.

The method has been applied to an experimental test case which coupled a physical cubic spring with a virtual mass-spring-damper system. The results showed that the proposed method helped to stabilize the filter with initially unstable filter behavior. The instability is caused by the high adaptation gain. The adaptation gain is updated as a reaction to the power-outflow from the actuator system and settles to a positive value. This allows the filter coefficient to converge such that the interface is synchronized. In other cases where adaptation with the chosen filter parameters is impossible such as for a high phase error of P_{gu}, the passivity constraint is maintained and the adaptation gain μ is taken down to zero. This means that the adaptation is still unable to fully mitigate the actuator dynamics but the power-flow methods proposed in this paper are still successful in preventing damaging behavior.

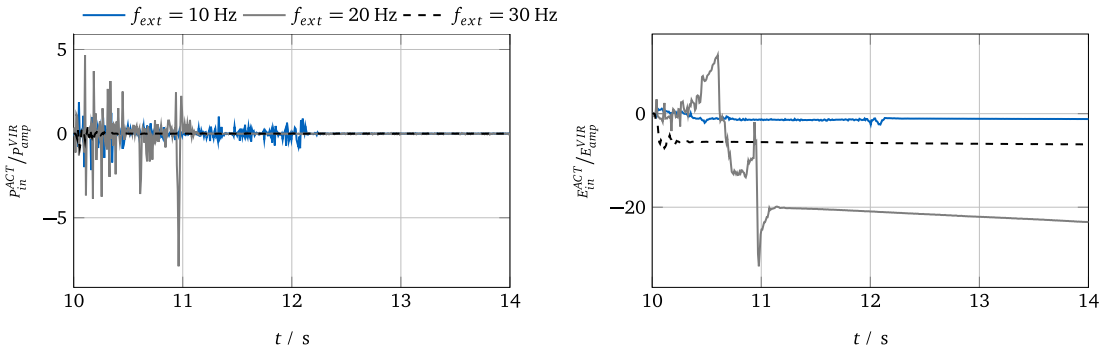

Figure 12: Power (left) and energy inflow (right) to actuator system with activated power-flow supervision.

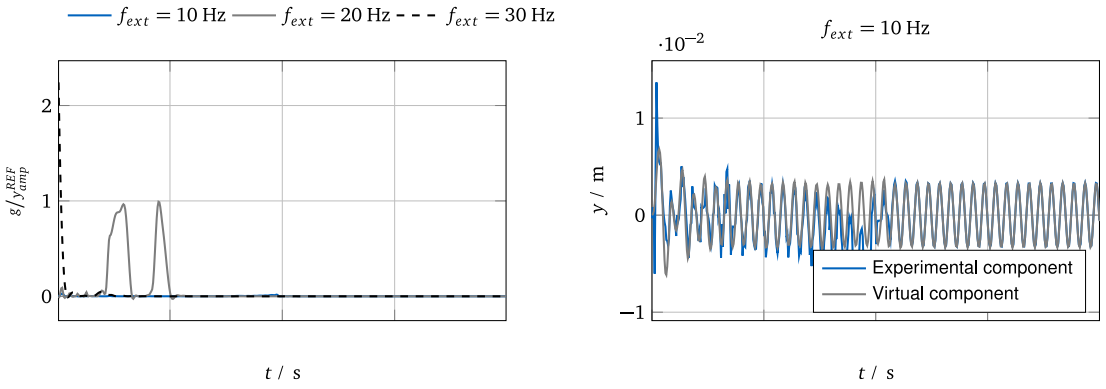

Figure 13: Learning curve (left) and interface synchronization (right) with activated power-flow supervision.The interface gap is normalized with the amplitude of the uncoupled interface displacement y_{amp}^{VIR}.

Conflict of interest

On behalf of all authors, the corresponding author states that there is no conflict of interest.

References

[1] Albu-Schäffer A, Ott C (2007) A Unified Passivity- based Control Framework for Position , Torque and Impedance Control of Flexible Joint. The International Journal of Robotics Research 26(1):23–29, DOI 10.1177/0278364907073776

[2] Anderson R, Spong M (1989) Anderson - 1989 - Bilateral Control of Teleoperators.pdf. IEEE Transactions on Automatic Control 34(2)

[3] Bartl A, Mayet J, Rixen D (2015) Adaptive Feedforward Compensation for Real Time Hybrid Testing with Harmonic Exciation. Proceedings of the 11th International Conference on Engineering Vibration (September):7–10

[4] Bartl A, Mayet J, Rixen D (2018) An adaptive approach to coupling vibration tests and simulation models with harmonic excitation. IEEE/ASME International Conference on Advanced Intelligent Mechatronics, AIM 2018-July:262–267, DOI 10.1109/AIM.2018.8452358

[5] Bayer V, Dorka U, Füllekrug U, Gschwilm J (2005) On real-time pseudo-dynamic sub-structure testing: algorithm, numerical and experimental results. Aerospace Science and Technology 9(3):223–232, DOI 10.1016/j.ast.2005.01.009

[6] du Bois J, Titurus B, Lieven N (2010) Transfer Dynamics Cancellation in Real-Time Dynamic Sub- structuring. In: Proceedings of ISMA 2010, pp 1891–1914

[7] Bolien M, Iravani P, du Bois J (2017) Toward Robotic Pseudodynamic Testing for Hybrid Simulations of Air-to-Air Refueling. IEEE/ASME Transactions on Mechatronics 22(2):1004–1013

[8] Bras JM (1999) Development of a Standardized Method for Actuator Characterization using Active Control of Impedance. Dissertation, Virginia Polytechnic Institute and State University

[9] Hannaford B, Ryu J (2002) Time-Domain Passivity Control of Haptic Interfaces. IEEE Transactions on Robotics and Automation 18(1):1–10

[10] Horiuchi T, Inoue M, Konno T, Namita Y (1999) Real-time Hybrid Experimental System with Actuator Delay Compensation and its Application to a Piping System with Energy Absorber. Earthquake Engineering and Structural Dynamics 28(10):1121–1141

[11] Wallace M, Wagg D, Neild S (2004) A Variable Leaky LMS Adaptive Algorithm. Conference Record of the Thirty-Eighth Asilomar Conference on Signals, Systems and Computers

[12] Kuo S., Morgan D.(1996) Active Noise Control Systems. John Wileys & Sons

[13] Niemeyer G, Slotine J (1991) Stable Adaptive Teleoperation. IEEE Journal of Oceanic Engineering 16(I)

[14] Peiris H, Plummer A, du Bois J (2018) Passivity Control in Real-time Hybrid Testing. 2018 UKACC 12th International Conference on Control (CONTROL) pp 317–322

[15] Peiris H, Plummer A, du Bois J (2020) Passivity Control for Nonlinear Real-time Hybrid Tests. Proceedings of the Institution of Mechanical Engineers, Part I: Journal of Systems and Control Engineering

[16] Plummer A (2006) Model-in-the-Loop Testing. Proceedings of the Institution of Mechanical Engineers, Part I: Journal of Systems and Control Engineering 220(3):183–199, DOI 10.1243/09596518JSCE207

[17] Stoten D, Li G, Tu J (2010) Model predictive control of dynamically substructured systems with application to a servohydraulically actuated mechanical plant. IET Control Theory & Applications 4(2):253–264

[18] Wagg DJ, Stoten DP (2001) Substructuring of dynamical systems via the adaptive minimal control synthesis algorithm. Earthquake Engineering & Structural Dynamics 30(6):865–877

[19] Wallace M, Wagg D, Neild S (2005) An adaptive polynomial based forward prediction algorithm for multi-actuator real-time dynamic substructuring. Proceedings of the Royal Society A: Mathematical, Physical and Engineering Sciences 461(2064):3807–3826, DOI 10.1098/rspa.2005.1532